EFFECT OF TEXTURAL FEATURES FOR LANDCOVER CLASSIFICATION OF UAV MULTISPECTRAL IMAGERY OF A SALT MARSH RESTORATION SITE

G. S. Norris [1,*], B. Leblon[1], A. LaRocque [1, *], M. A. Barbeau[2], A. R. Hanson[3]

[1]Faculty of Forestry and Environmental Management, University of New Brunswick, Fredericton, NB, Canada, E3B 5A3 (gnorris1, bleblon, larocque)@unb.ca
[2]Department of Biology, University of New Brunswick, Fredericton, NB, Canada, E3B 5A3 - mbarbeau@unb.ca
[3] Canadian Wildlife Service, Environment Canada, P.O. Box 6227, Sackville, NB, Canada, E4L 4N1 - al.hanson@canada.ca

KEY WORDS: coastal restoration, UAV, Micasense Dual-Camera System, vegetation indices, textural features, Random Forests, Pix4D, Bay of Fundy

ABSTRACT:

Salt marshes are intertidal ecosystems valuable for services including coastal protection and carbon sequestration. Restoration of salt marshes is popular in this era of climate change and sea-level rise, especially in areas where marshes have been historically altered, including in the Bay of Fundy. Salt marsh restoration involves landcover change through time as a community of halophytic vegetation develops in the study area. Restoration sites are difficult to survey using traditional on-foot methods, and developing remote sensing methods to survey them would increase efficiency of monitoring. The purpose of our study was to assess the capability of UAV multispectral imagery to map landcovers in a salt marsh restoration site in the Musquash Estuary, New Brunswick, Canada. We used the Random Forests (RF) supervised classifier and validated our maps using field data. We also evaluated the importance of textural features by running two classifications, with and without textural features. The classification omitting textural features had lower classification and validation accuracies (96.29 % and 91.23 %, respectively) than the classification and validation accuracies obtained by including textural features (99.56 % and 96.84 %, respectively). Additional work is required to test our method in different locations and seasons.

1. INTRODUCTION

Salt marshes are intertidal ecosystems found globally that provide valuable services, including coastal protection, carbon sequestration, and habitat for many species of birds, mammals, fish, and invertebrates (Gedan, Silliman, Bertness, 2009). In the past, salt marshes were converted for agricultural land, freshwater impoundments, or other anthropogenic use. An estimated 50 % of salt marshes worldwide and 85 % of those in the Bay of Fundy (in Atlantic Canada) have been lost or degraded. (Thomas, 1983; Barbier et al., 2011). There is interest in salt marsh restoration to increase ecosystem services that are becoming more valuable in an era of climate change and sea-level rise (Roman, Burdick, 2012). Many dikes protecting converted salt marshland in the Bay of Fundy and beyond are at or near the end of their lifespan, and salt marsh restoration is a possible management option.

Mapping salt marsh restoration sites is important to determine the restoration trajectory, assess the value of ecosystem services as they develop, model vegetation dynamics, and plan future projects. Without proper planning, a salt marsh restoration may fail, and the area is converted into a mudflat habitat, as seen elsewhere (French, 2006). Salt marshes can be challenging to survey with traditional field methods, especially when they are in restoration. Indeed, they can be very large, are characterized by halophytic vegetation on potentially unconsolidated soft sediment, show striking zonation, and have geomorphological features including creeks and salt pools that can be difficult to cross (Bertness, 2007). Because of this, field-surveying salt marsh restoration sites is time-consuming and has relatively low efficiency. Currently, available remote sensing technology, specifically images acquired with unmanned aerial vehicles (UAV), can be used to examine biological and geological features in environments that are time-consuming and difficult to monitor via field survey, such as salt marshes (Ridge, Johnston, 2020). UAV images have become increasingly popular as a tool for ecological monitoring thanks to advancements in UAV technology, compatible multispectral sensors, and computer software for processing large datasets (Fonstad et al., 2013; Larrinaga, Brotons, 2019). Vegetation has high reflectance in the red edge and near-infrared electromagnetic spectra, and using multispectral sensors with such wavebands makes it possible to discriminate plant species, density, and physiological state using UAV imagery (Lorenzen, Jensen, 1988; Elvidge, 1989; Peñuelas, Filella, 1998). UAV imagery has the additional advantage of a very high spatial resolution because UAVs can operate at much lower altitudes than conventional aircraft and spacecraft (Colomina, Molina, 2014; Pajares, 2015). This is useful because salt marsh zonation and other vegetation changes typically occur at spatial resolutions of centimeters (Doughty, Cavanaugh, 2019).

The first studies using UAV imagery over salt marshes were about sedimentation/erosion (Delcourt et al. 2009; Hugenholtz et al., 2013), or mapping vegetation communities with images acquired in the red, green, and blue bands (RGB) alone (Wan et al., 2014) or with the near-infrared (NIR) band (Martin et al., 2018). More recently, multispectral UAV imagery has been used to map vegetation communities (Dale et al., 2020; Villoslada et al., 2020; Nardin et al., 2021) or inundated areas (Sarira et al., 2020), quantify vegetation height (DiGiacomo et al., 2020) or biomass (Doughty, Cavanaugh, 2019), model wave attenuation (Mury et al., 2020), and assess ecosystem productivity (Diaz-Delgado, Cazacu, Adamescu, 2018).

Most studies using multispectral UAV imagery over salt marshes have only considered the spectral information of the images, including vegetation indices. Adding textural information can also be helpful (Xu et al., 2020), particularly with high spatial resolution imageries (Mishra et al., 2018), such as UAV imagery. To date, few studies have been

* Corresponding authors

conducted in salt marsh ecosystems investigating the potential of using textural features with multispectral UAV imagery for landcover mapping. Kelcey and Lucieer (2013) showed the benefits of using textural features when mapping salt marshes with UAV RGB imagery. In a freshwater wetland mapping study, Li et al. (2021) found that calculating textural features using multispectral bands, including those among the RedEdge spectrum, was as valuable as calculating them using visible RGB bands.

The objectives of the present study were to use UAV multispectral imagery to classify a variety of landcovers in a salt marsh restoration site located in the Musquash Estuary, New Brunswick, Canada, and investigate the use of textural features during classification. We used Random Forests (RF), a non-parametric supervised classifier (Breiman et al., 2001) that outperforms the Maximum Likelihood Classifier (MLC) (Ok, Akar, Gungor, 2012; He et al., 2015). Our study is an essential step for developing a methodology that we will use to monitor the critical stages of salt marsh restoration in Atlantic Canada. The following restoration stages were identified: previous vegetation die-off, establishment of *Spartina alterniflora*, and establishment of a high marsh (including *S. patens*, etc.), resulting in a salt marsh with distinct zonation (Boone et al., 2017; Virgin et al., 2020).

2. MATERIALS AND METHODS

2.1 Study area

The study area is in the Musquash Estuary (Latitude: 45°10'54" N, Longitude: 66°19'42" W; Figure 1), which drains into the Bay of Fundy, and has approximately 773 hectares of vibrant salt marsh. Since the study area is in the uppermost portion of the estuary (~10 km from the Bay), the salt marsh communities are comprised of a mix of halophytic and semi-halophytic (brackish) vegetation with varying inundation tolerances (Greenlaw, Schumacher, McCurdy, 2014; Norris et al., 2020), and are more diverse than salt marshes located directly on the Bay of Fundy (Virgin et al., 2020). *Spartina* (syn. *Sporobolus*) grasses (namely *Spartina alterniflora, S. patens, S. pectinata*) are key community members in most salt marshes of the region, including in the Musquash Estuary, and have been foundational during other restoration projects (Boone et al., 2017; Virgin et al., 2020).

While considered to be one of the estuarine ecosystems in Maritime Canada least impacted by humans (Fisheries and Oceans Canada, 2017), lands in the Musquash Estuary (like most other salt marshes in the Bay of Fundy) were subject to anthropogenic impact after European colonization in the 17th century (Thompson, 2001). In addition, in the 1960s and 1970s, 136 hectares of marsh were diked for cattle pasture (Thompson, 2001). Ducks Unlimited Canada was given these diked pasture lands in the early 1980s and, after repairing the failing tidal gates, created freshwater impoundment and marsh habitat for waterfowl at that time (Greenlaw, Schumacher, McCurdy, 2014). Plant communities in these freshwater impoundments include species of bulrush (cattails *Typha* spp. and soft stem bulrush *Schoenoplectus tabernaemontani*) and other brackish and freshwater plants (Mallik, Wein, 1986).

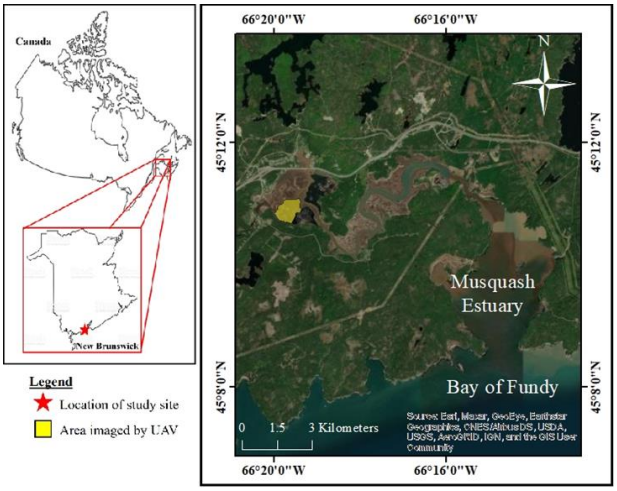

Figure 1. Location of the study area and limits of the area imaged by the UAV imagery over a Google Earth image.

Given the now acknowledged benefits of salt marshes (Gedan, Silliman, Bertness, 2009) and the protected status of the Musquash Estuary (Greenlaw, Schumacher, McCurdy, 2014; Fisheries and Oceans Canada 2017), there is interest in reverting the freshwater impoundments back to natural salt marshes. The restoration of Musquash's northwestern freshwater impoundment (Figure 1) began on 29 January 2019 when the dike was mechanically breached in at least 2 locations, allowing the impoundment to drain (Norris et al., 2020). At the time of our study, the restoration was in its second year.

2.2 Image acquisition

Multispectral images were acquired using a MicaSense Dual Camera System (*MicaSense, 1300 N. Northlake Way, Suite 100, Seattle, Washington, 98103, USA*) mounted to a DJI Matrice V2 UAV (*DJI, No.18 Gaoxin South 4th Ave, Nanshan District, Shenzhen, 518057, China*). The camera has ten bands covering the visible and near-infrared spectra (Table 1). Images were acquired with 80 % front and side overlap between them along with a grid pattern over the sites at 100 m altitude using DJI Pilot mission planner software. The images were taken on 5 July 2020 (Table 2), after vegetation had been growing for a few months. Each image had a spatial resolution close to 7 cm.

Table 1. Spectral characteristics of the ten bands acquired by the MicaSense Dual-Camera system.

Band number	Band name	Center wavelength (µm)	Bandwidth (µm)
1	Blue444	444	28
2	Blue475	475	32
3	Green531	531	14
4	Green560	560	27
5	Red650	650	16
6	Red668	668	14
7	RedEdge705	705	10
8	RedEdge717	717	12
9	RedEdge740	740	18
10	NIR842	842	57

Table 2. Characteristics of the UAV imagery used and related environmental conditions during acquisition.

Variable	Value
Acquisition date:	2020/07/05
Flight commencement time:	14:40
Tidal height (m)	5.3
Cloud cover (Type: % coverage):	Stratus: 100
Solar azimuth (°):	218
Solar elevation (°)**:**	63
Air temperature (°C):	12
Relative humidity (%):	100
Wind speed (km h^{-1}):	6
Wind direction:	SE
UAV altitude (m AMSL*):	100
UAV speed (m s^{-1}):	10
UAV course angle **(°)**:	116
Overlap between adjacent images (%):	80
Imaged acquired (number):	9162
Image spatial resolution (cm):	~7

(*) AMSL = Above Mean Sea Level (2) Weather data collected from Point Lepreau weather station (Latitude: 45°4'12" N Longitude: 66°27'0" W)

2.3 Field data

Ground truth observations were obtained on 28 June 2020 using stratified random sampling with three transects and 15 quadrats (0.5 m x 0.5 m) per transect. Observations were also made in several focus locations along the site's perimeter. In each quadrat, the landcover class was determined. Quadrat locations were marked with GPS coordinates using a Garmin GPS 73 handheld navigator (*Garmin Ltd., 1200 E 151st St, Olathe, Kansas, 66062, USA*). These GPS ground-truthed locations were used to validate the resulting map in ArcMap® (*ESRI, 380 New York Street, Redlands, California, USA*). We used a total of 285 validation points of 14 classes (19¬22 points/class; Table 3, Figure 2).

Table 3. Number of training areas and validation points per landcover class.

Class #	Class name	Training areas (pixels)	Validation points
1	Deep estuary water	1,150	20
2	Submerged bare mud	675	21
3	Submerged vegetated mud	1,171	20
4	Bare mud	1,289	19
5	Green algae	817	20
6	Dwarf spike rush	2,890	20
7	Deep salt pool water	928	22
8	Dead vegetation	1,264	21
9	Cattail roots	2,424	20
10	Cattail stems	1,356	20
11	Soft stem bulrush	3,236	20
12	Terrestrial vegetation (light)	1,570	21
13	Terrestrial vegetation (dark)	836	20
14	Halophytes and semi-halophytes	1,720	21
	Total	21,326	285

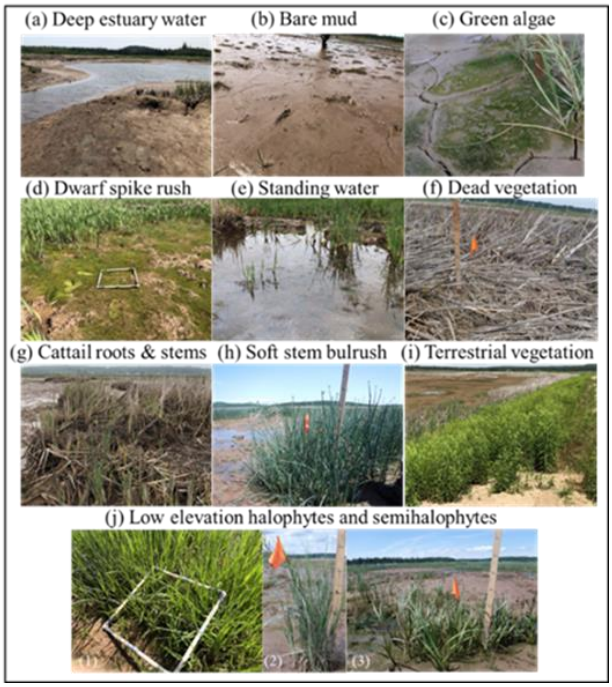

Figure 2. Ground photographs for the following landcover classes: a) deep estuary water, b) bare mud, c) green macroalgae (Chlorophyta), d) dwarf spike rush (*Eleocharis parvula*), e) cloudy standing water, f) dead vegetation, g) cattail (*Typha* spp.) roots and stems, h) soft stem bulrush (*Schoenoplectus tabernaemontani*), i) terrestrial vegetation (light), and j) low elevation halophytes and semi-halophytes (1: *Bolboschoenus maritimus*, 2: *Spartina pectinata*, 3: *Spartina alterniflora*).

2.4 Pre-classification image processing

The processing workflow of the images (Figure 3) first included georeferencing and mosaicking together the individual UAV images corresponding to similar bands using Pix4Dmapper software (*Pix4D, Route de Renens 24, 1008 Prilly, Switzerland*). The resulting image mosaics were used to compute vegetation indices and textual features using an EASI script in the PCI Geomatica Banff® software (*PCI Geomatics Group Inc., 50 West Wilmot Street, Richmond Hill, Ontario, Canada*). The 28 vegetation indices used in our study were selected because they have been valuable in previous vegetation mapping studies. Textural features contain information about the spatial distribution of tonal variations within an image. Textural features are calculated in a variety of different manners by relating the spectral tone of one pixel in the imagery to its nearest neighbors using gray-level co-occurrence matrices (GLCM) (Haralick, Shanmugam, Dinstein, 1973). The reflectance values of each MicaSense image mosaic were represented by gray levels, with zero corresponding to "black" and higher values corresponding to lighter shades. The GLCM examines the spatial relationship among pixels within a defined kernel size. For our study, the kernel size was set to 9. The kernel moves iteratively across the image, covering each pixel. A matrix is derived from the frequency of gray level (pixel value) pair co-occurrence at each pixel location. From each GLCM, several different measures of texture can then be extracted. In our study, we calculated ten textural features per MicaSense band for a total of 100 (Table 4).

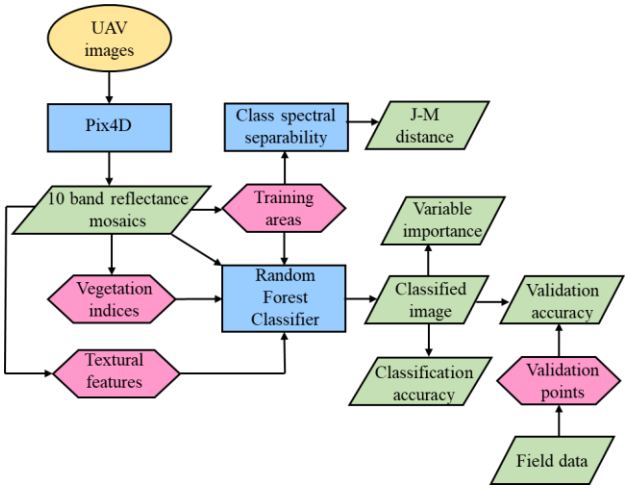

Figure 3. Flowchart of the method used for processing the UAV images.

Table 4. Textural features calculated for each of the ten MicaSense bands (adapted from Haralick et al., 1973).

Textural feature	Formula
Homogeneity	$\sum_{i=0}^{N-1}\sum_{j=0}^{N-1}\frac{P(i,j)}{1+(i-j)^2}$
Contrast	$\sum_{i=0}^{N-1}\sum_{j=0}^{N-1}P(i,j)*(i-j)^2$
Dissimilarity	$\sum_{i=0}^{N-1}\sum_{j=0}^{N-1}P(i,j)*\lvert i-j\rvert$
Mean	$\sum_{i=0}^{N-1}\sum_{j=0}^{N-1}i*P(i,j)$
Standard deviation	$\left[\sum_{i=0}^{N-1}\sum_{j=0}^{N-1}P(i,j)*(i-\mu i)^2\right]^{1/2}$
Entropy	$\sum_{i=0}^{N-1}\sum_{j=0}^{N-1}-P(i,j)*\log_e(P(i,j))$
Angular second moment	$\sum_{i=0}^{N-1}\sum_{j=0}^{N-1}P(i,j)^2$
Angular correlation	$\sum_{i=0}^{N-1}\sum_{j=0}^{N-1}\frac{P(i,j)*(i-\mu i)*(j-\mu j)}{\sigma i*\sigma j}$
GLDV angular second moment	$\sum_{i=0}^{N-1}V(k)^2$
GLDV entropy	$\sum_{i=0}^{N-1}(-V(k))*\log_e(V(k))$

N = number of grey levels. $P(i,j)$ = probability of values i and j occurring in adjacent pixels in the original image within the window defining the neighbourhood. i = DN value of a target pixel, j is the DN value of its immediate neighbour, μ = mean, σ = standard deviation, V= value of the pixel.

2.5 Image classification and accuracy assessment

Training areas were delineated for each landcover class over the imagery. A total of 21,326 pixels were delineated for the 14 classes (Table 3). Training areas typically had a size of 5 by 5 pixels, although there were exceptions due to heterogeneous landcovers. The PCI Geomatica Banff® software was used to compute the Jeffries–Matusita (J-M) distance between class pairs, which measures class spectral separability. J-M distance values range from 0 to 2, with values of 2 representing classes that are entirely separated (Richards, Jia, 1999). The J-M distance computations included only the ten MicaSense band reflectance values. The training areas were input into the Random Forest (RF) classifier. Two classifications were done: one omitting textural features (38 input features including MicaSense bands and vegetation indices), and one including them (138 input features). The RF classifiers produced classification accuracies (based on the training areas), the classified images, and the importance rankings of the input features (including the MicaSense bands, vegetation indices, and textural features) (Waske, Braun, 2009; Louppe et al., 2013; Gislasson, Benediktsson, Sveinsson, 2006; Strobl et al., 2008). Rankings are based on each variable's mean decrease accuracy or Gini during the classification. The mean decrease in accuracy expresses how much accuracy the model loses by excluding each variable; the more accuracy suffers, the more important the variable is (Han, Guo, Yu, 2016). The mean decrease Gini coefficient measures how each variable contributes to the homogeneity of the nodes and leaves in the Random Forest (Han, Guo, Yu, 2016). Validation accuracies were computed by comparing the classified images to the validation points.

3. RESULTS

3.1 Landcover class spectral separability

The landcover classes used in the classifications were well separated, indicated by an average J-M distance of 1.98 between class pairs (Table 5). The highest separability values of 2.00 were between 61 of the 91 landcover class pairs (67.0 %), indicating that they were completely separated. The deep estuary water, bare mud, dead vegetation, and halophytes and semi-halophytes classes were very well separated (J-M distance values > 1.98) from all other classes. Relatively low separability values were computed for class pairs including different types of vegetation. The lowest separability (1.77) was between the cattail stems and soft stem bulrush classes. Other class pairs with low separability (< 1.90) included soft stem bulrush and dark terrestrial vegetation (1.78), and the two terrestrial vegetation classes (1.88).

Table 5. Fifteen (of 91) lowest Jeffries–Matusita (J-M) distances for landcover classes computed using the ten bands of the UAV imagery.

Class#1	Class #2	J-M Distance
10	11	1.77
11	13	1.78
12	13	1.88
10	12	1.90
3	5	1.90
6	9	1.94
3	6	1.95
6	10	1.95
9	10	1.95
10	13	1.95
2	3	1.96
5	6	1.96
3	7	1.96
6	11	1.96
1	7	1.98
Overall mean		1.98

3.1 Classification

Classifications were executed with and without textural features. Both classifications achieved excellent overall accuracies, with the classification omitting texture achieving a lower accuracy (96.3 %; Table 6) than the classification including texture (99.6 %; Table 6). For the classification omitting textural features, the lowest User's (UA) and Producer's accuracies (PA) corresponded to the cattail stems (UA: 87.8 %, PA: 89.7 %) and the low elevation halophytes and

semi-halophytes (UA: 89.9 %, PA: 87.3 %). The cattail stems class also corresponded to the lowest UA and PA for the classification that included textural features (UA: 98.2 %, PA: 98.5 %). The low accuracies of these classes are due to confusion with the other vegetation classes. Confusion between vegetation types has been common in previous salt marsh classifications (Belluco et al., 2006; Hladik, Alber, 2014; van Beijma et al., 2014; Gray et al., 2018; Meng et al., 2018).

Table 6. Classification and validation accuracies for each landcover class when omitting and including textural features.

Classifier	**Texture omitted**				**Texture included**			
Class	Classification		Validation		Classification		Validation	
	UA	**PA**	**UA**	**PA**	**UA**	**PA**	**UA**	**PA**
1	99.7	100	90.9	100	100	100	95.2	100
2	100	99.9	100	95.2	100	100	100	100
3	99.1	98.5	100	90.0	99.7	100	95.0	95.0
4	99.8	99.5	100	100	99.9	99.9	100	100
5	98.5	98.7	81.8	90.0	99.9	99.6	100	95.0
6	96.8	97.5	78.3	90.0	99.6	99.5	95.0	95.0
7	99.6	100	100	94.5	100	100	100	95.5
8	99.6	99.5	100	95.2	99.9	99.8	100	100
9	98.4	97.2	95.2	100	99.7	99.6	100	100
10	87.8	89.9	81.8	90.0	98.2	98.5	100	95.0
11	96.0	95.4	83.3	75.0	99.7	99.6	100	100
12	94.7	97.0	95.0	90.5	99.4	99.8	90.9	95.2
13	92.0	93.1	85.0	85.0	98.8	100	100	85.0
14	89.7	87.3	89.5	81.0	99.3	98.6	84.0	100
OA	96.3		91.2		99.6		96.8	

UA = User's Accuracy (%); PA = Producer's Accuracy (%); OA = Overall Accuracy (%).

The most important input features for the classification omitting texture included the ten MicaSense bands in the top 14 and 18 out of 38 when ranking the highest mean decrease accuracy and mean decrease Gini values, respectively. The MicaSense bands with the greatest mean decrease accuracy values were the RedEdge705, RedEdge717, and Red668. The bands with the greatest mean decrease Gini were the Red668, Green531, and NIR842. The vegetation indices with the largest mean decrease accuracy and Gini values were the NDRE.3 and RERVI.3.

For the classification including texture, of the 30 input features with the highest mean decrease accuracy values, 24 were textural features. Of these 24, ten were calculated using the RedEdge717 band. Calculating textural features using RedEdge bands has been helpful in previous freshwater wetland mapping studies (Li, Zhao, Xu, 2021). The lowest ranking textural features in our classification (of 138 total input features) were calculated using the RGB bands, which in Li et al. (2021) were found to have similar importance to textural features calculated using the RedEdge bands. The most important method of calculating textural features was the Mean calculation. All 10 Mean textural features (1 value per band) were within the top 53 in mean decrease accuracy and the top 45 in mean decrease Gini.

3.2 Validation

We achieved overall validation accuracies greater than 90.0 % for both classifications, but the accuracy was slightly lower when we omitted textural features (91.2 %; Table 6) than when we included them (96.8 %; Table 6). For the classification omitting textural features, the class with the highest error of commission (EC; 22.0 %) was the dwarf spike rush class. Other classes with EC greater than 10.0 % were the following: green algae, cattail stems, soft stem bulrush, terrestrial vegetation, and halophytes and semi-halophytes. Classes with the highest user's accuracy of 100 % included submerged bare mud, submerged vegetated mud, bare mud, cloudy standing water, and dead vegetation. The class with the highest error of omission was the soft stem bulrush class, and other classes with relatively high errors of omission (EO) were terrestrial vegetation and halophytes and semi-halophytes. Classes with the highest producer's accuracy of 100 % were deep estuary water, bare mud, and cattail roots. For the classification including texture, classes with both 100 % UA and PA included submerged bare mud, bare mud, dead vegetation, cattail roots, and soft stem bulrush. The class with the highest EC was the halophytes and semi-halophytes class. The class with the highest EO was the dark terrestrial vegetation class. Confusion between vegetation classes was greater in the classification that omitted textural features. The validation accuracy of the soft stem bulrush class was the most improved after incorporating the textural features into the classification. User's accuracies of the halophytes and semi-halophytes classes were lower in the classification using textural features.

4. DISCUSSION

The two resulting classified images from our study both displayed many heterogeneous vegetation patches with multiple species (Figure 4). They showed that most of the study area was covered by dwarf spike rush, cattail roots, green algae, bare mud, and submerged vegetated mud (Table 7, Figure 4). The restoration project was in its second year at the time of image acquisition. Not surprisingly, vegetation present on-site before restoration (cattails, soft stem bulrush) were stressed (and dead in many areas) by the reintroduction of tidal flow at the beginning of restoration. The site contained many bare areas, similar to what was observed during the early years of another project located in the Bay of Fundy (Boone et al., 2017; Virgin et al., 2020). We observed opportunistic brackish species of vegetation (dwarf spike rush, green algae, etc.) growing in the study area. Detection of halophytic vegetation growing in the restoration site in the second year of restoration was promising. We expect that as the restoration progresses, the amount of halophytic vegetation will increase as it spreads and outcompetes the small opportunistic species. The terrestrial vegetation classes covered the least area in the thematic images and were restricted to a high elevation "island" area near the center of the study area (Table 7; Figure 4). The landcovers that had similar areas (within 1,000 m^2) after classifications with and without textural features included submerged bare mud, cloudy standing water, dead vegetation, soft stem bulrush, and both terrestrial vegetation classes. The classes that increased (by more than 1,000 m^2) in area after using texture were dwarf spike rush, cattail roots, cattail stems, and halophytes and semi-halophytes. The deep estuary water, submerged vegetated mud, bare mud, and green algae classes decreased in area after including texture (Table 7). The total landcover area of the two classifications were slightly different, likely from pixels along the edge of the imagery being differently classified into the "null" class ("null" class not presented).

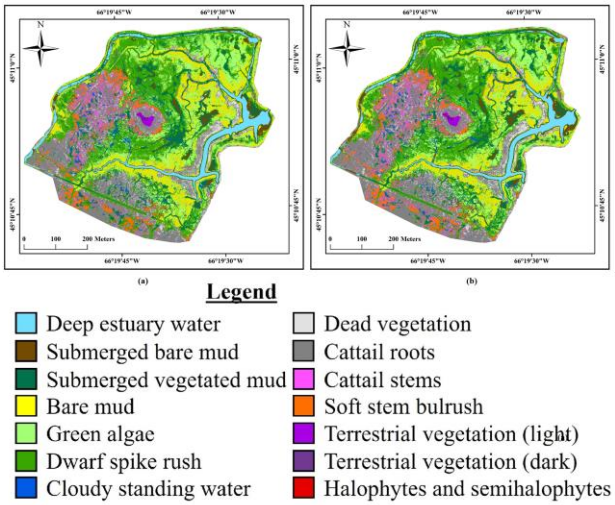

Figure 4. Classified image of the Musquash restoration site produced with the Random Forest classifier applied to (a) 38 spectral bands and vegetation indices, and (b) 138 spectral bands, vegetation indices, and textural features of the UAV imagery.

Table. 7. Area of each landcover class extracted from the classified images.

Class #	Class name	Area (m^2)	
		Texture omitted	Texture included
1	Deep estuary water	17912	16066
2	Submerged bare mud	11918	12844
3	Submerged vegetated mud	35429	31321
4	Bare mud	46277	42804
5	Green algae	52754	49868
6	Dwarf spike rush	85130	87811
7	Cloudy standing water	7258	7254
8	Dead vegetation	13078	13172
9	Cattail roots	56908	61448
10	Cattail stems	12396	16578
11	Soft stem bulrush	12813	12379
12	Terrestrial vegetation (light)	878	902
13	Terrestrial vegetation (dark)	289	253
14	Halophytes and semi-halophytes	2150	2,474
	Total	355191	355174

By combining UAV multispectral imagery and field survey, we were able to accurately discriminate landcovers based on spectral and textural features of the imagery. Identifying landcovers in a salt marsh restoration site can be a helpful tool when evaluating a project's restoration trajectory and status. As introduced above, critical stages of salt marsh restoration have been identified in a nearby, fully saline, salt marsh restoration project in Aulac (Boone et al., 2017; Virgin et al., 2020). In this salt marsh, stages of restoration included previous vegetation die-off (*S. pectinata*), colonization and spread of bioengineering halophytes (*S. alterniflora*), and finally colonization of high-elevation halophytes (including *S. patens*) and formation of distinct marsh zonation (Virgin et al. 2020). The classification used in the present study would be unable to identify these stages because key species *S. pectinata* and *S. alterniflora* were grouped together in the "halophytes and semi-halophytes" class. Nevertheless, our classified landcover maps for the Musquash site, which has more vegetation diversity (includes brackish species) than the Aulac site is still helpful to assess its restoration trajectory. We identified previous vegetation as cattails (*Typha* spp.) and soft-stem bulrush (*Schoenoplectus tabernaemontani*) in the early Musquash restoration, which has also been the case during other restorations of freshwater impoundments up estuaries within the Bay of Fundy region (Bowron et al., 2012). Our landcover maps can monitor the die-off of previous species by distinguishing between their live and dead stems. In addition, our identification of *S. pectinata* and *S. alterniflora* as a grouped-landcover class is useful in determining early aspects of a restoration trajectory for a site relatively high up an estuary (we are discovering that opportunisitic brackish plants play a more prominent role in the early recovery trajectory of such sites). Since our Musquash restoration project was young at the time of image acquisition, few patches of *S. pectinata* and *S. alterniflora* were available, and even fewer of the high-elevation halophyte *S. patens*, for training the imagery. Based on previous restorations in the Bay of Fundy region (Bowron et al., 2011; Bowron et al., 2012; Virgin et al., 2020), we expect a greater area of *Spartina* grasses and so more area to train our classification algorithm and distinguish between these and other halophytic species in oncoming years for the Musquash restoration. Another line of work will be to classify multispectral imagery of salt marsh restoration projects located in more saline sites (where the *Spartina* grasses are more dominant community members) to help distinguish between the various halophytic and semi-halophytic species in the imagery. To summarize, our classification algorithms used in the present study are useful in identifying the stages of salt marsh restoration in our study area at the time of acquisition. However, more work must be done at different times of the year and in other locations to refine our algorithm so it can be used in many salt marsh situations.

5. CONCLUSIONS

Mapping vegtation in salt marsh restoration sites is important to determine the trajectory of the restoration, assess the value of ecosystem services as they develop, model vegetation dynamics, and plan future projects. Field sampling methods that have been traditionally used to monitor salt marsh restoration are time-consuming and do not evaluate the entire site in the way remotely sensed imagery does. Our study has shown the potential of applying a Random Forests classifier to UAV multispectral images to produce accurate landcover maps showing the distribution of different vegetation types in a salt marsh restoration site in the Musquash Estuary. The study area's classification and validation accuracies were improved after incorporating textural features into the RF classification. Future work is needed to determine how seasonal and site differences affect landcover classification in salt marsh restoration sites. Also, testing the methodology in natural salt marsh sites to assess ecosystem health and quality of services will provide comparisons for those undergoing restoration.

6. ACKNOWLEDGEMENTS

We thank Eleanor Gallant, Julianne Richard, and Lyle Vicaire for assisting in the field. We thank Nic McLellan (NRM), Wade Lewis, and Adam Campbell from Ducks Unlimited Canada (DUC), and Dr. Jeff Ollerhead from Mount Allison University for information. The research was supported by Ducks Unlimited Canada, NB Department of Transportation and Infrastructure, Fisheries and Oceans Canada (Small Craft Harbours), a MITACS ACCELERATE Fellowship (GSN, MAB, BL, NRM), the Natural Sciences and Engineering Research Council of Canada (Discovery grant to MAB, and a CREATE grant to BL), the NB Environmental Trust Fund (Project #200133 and #210235 grants to AL, BL, MAB, GSN),

the Canada Summer Jobs Program (Employment and Social Development Canada), and the University of New Brunswick.

7. REFERENCES

Barbier, E.B., Hacker, S.D., Kennedy, C., Koch, E.W., Stier, A.C., Silliman, B.R., 2011. The value of estuarine and coastal ecosystem services. *Ecol Monogr*, 81, 169–193.

Belluco, E., Camuffo, M., Ferrari, S., Modenese, L., Silvestri, S., Marani, A., Marani, M., 2006. Mapping salt-marsh vegetation by multispectral and hyperspectral remote sensing. *Remote Sens Env*, 195(1), 5467.

Bertness, M.D., 2007. Atlantic Shorelines: Natural History and Ecology. Princeton University Press, Princeton, New Jersey.

Breiman, L., 2001. Random forests. *J Mach Learn*, 45(1), 5–32.

Boone, L.K., Ollerhead, J., Barbeau, M.A., Beck, A.D., Sanderson, B.G., Mclellan, N.R., 2017. Returning the tide to dikelands in a macrotidal and ice-influenced environment: challenges and lessons learned. In: Coastal Wetlands: Alteration and Remediation. Springer International Publishing AG, Cham, Switzerland, 705–749.

Bowron, T.M., Neatt, N., van Proosdij, D., Lundholm, J., Graham, J. 2011. Macro-tidal salt marsh ecosystem response to culvert expansion. *Rest Ecol*, 19(3), 301–322.

Bowron, T.M., Neatt, N., van Proosdij, D., Lundholm, J. 2012. Salt marsh tidal restoration in Canada's Maritime Provinces. In: Tidal Marsh Restoration: A Synthesis of Science and Management. Island Press, Washington, DC, 191–209.

Colomina, I., Molina, P. 2014. Unmanned aerial systems for photogrammetry and remote sensing : A review. *Int Soc Photogramme*, 92, 79–97.

Delacourt, C., Allemand, P., Jaud, M., Grandjean, P., Deschamps, A., Ammann, J., Cuq, V., Suanez, S. 2009. DRELIO: An unmanned helicopter for imaging coastal areas. *J. Coastal Res*, 1489-1493.

Dale, J., Burnside, N.G., Hill-Butler, C., Berg, M.J., Strong, C.J., Burgess, H.M., 2020. The use of unmanned aerial vehicles to determine differences in vegetation cover: a tool for monitoring coastal wetland restoration schemes. *Remote Sens*, 12(24), 40224038.

Díaz-Delgado, R., Cazacu, C., Adamescu, M. 2018. Rapid assessment of ecological integrity for LTER wetland sites by using UAV multispectral mapping. *Drones* 3, 3.

DiGiacomo, A.E., Bird, C.N., Pan, V.G., Dobroski, K., Atkins-Davis, C., Johnston, D.W., Ridge, J.T. 2020. Modeling salt marsh vegetation height using unoccupied aircraft systems and structure from motion. *Remote Sens*, 12(14), 23332350.

Doughty, C.L., Cavanaugh, K.C. 2019. Mapping coastal wetland biomass from high resolution Unmanned Aerial Vehicle (UAV) imagery. *Remote Sens*, 11, 540, https://doi.org/10.3390/rs11050540.

Elvidge, C.D., 1989. Visible and near infrared reflectance characteristics of dry plant material. *Int J of Remote Sens*, 11, 1775–1795.

Fisheries and Oceans Canada, 2017. Musquash Estuary: a Management Plan for the Marine Protected Area and Administered Intertidal Area. Dartmouth, NS, 53 pg.

Fonstad, M.A., Dietrich, J.T., Courville, B.C., Jensen, J.L., Carbonneau, P.E. 2013. Topographic structure from motion: A new development in photogrammetric measurement. *Earth Surf Process Landf*, 38, 421–430.

French, P.W., 2006. Managed realignment – the developing story of a comparatively new approach to soft engineering. *Estuarine and Coastal Shelf Science*, 67, 409–423.

Gedan, K.B., Silliman, B.R., Bertness, M.D., 2009. Centuries of human-driven change in salt marsh ecosystems. *Ann Rev Mar Sci*, 1, 117–141.

Gislason, P.O., Benediktsson, J.A., Sveinsson, J.R., 2006. Random Forests for land cover classification. *Pattern Recogn. Lett*. 27(4), 294–300.

Gray, P.C., Ridge, J.T., Poulin, S.K., Seymour, A.C., Schwantes, A.M., Swenson, J.J., Johnston, D.W., 2018. Integrating drone imagery into high resolution satellite remote sensing assessments of estuarine environments. *Remote Sens*, 10(8), 12571281.

Greenlaw, M.E., Schumacher, M.N., McCurdy, Q.M., 2014. A habitat map and updated high water boundary of the Musquash Estuary. Canadian Technical Report of Fisheries and Aquatic Sciences, 3093, 26 pg.

Han, H., Guo, X., Yu, H., 2016. Variable selection using mean decrease accuracy and mean decrease Gini based on random forest. *7th IEEE international conference on software engineering and service science (ICSESS)*, 219-224.

Haralick, R.M., Shanmugam, K., Dinstein, I., 1973. Textural features for image classification. *IEEE Sys Man Cybern*, 3(6), 610¬621.

He, J., Harris, J.R., Sawada, M., Behnia, P. 2015. A comparison of classification algorithms using Landsat-7 and Landsat-8 data for mapping lithology in Canada's Arctic. *International Journal of Remote Sens*, 36(8), 22522276, doi:10.1080/01431161.2015.1035410.

Hladik, C., Alber, M., 2014. Classification of salt marsh vegetation using edaphic and remote sensing-derived variables. *Estuar Coast Shelf S*, 141, 4757.

Hugenholtz, C.H., Whitehead, K., Brown, O.W., Barchyn, T.E., Moorman, B.J., LeClair, A., Riddell, K., Hamilton, T 2013.. Geomorphological mapping with a small unmanned aircraft system (sUAS): Feature detection and accuracy assessment of a photogrammetrically-derived digital terrain model. *Geomorphology*, 194, 16–24.

Kelcey, J., Lucieer, A., 2013. An adaptive texture selection framework for ultra-high resolution UAV imagery. In *2013 IEEE International Geoscience and Remote Sensing Symposium-IGARSS*, 38833886.

Larrinaga, A.R.; Brotons, L. Greenness Indices from a Low-Cost UAV Imagery as Tools for Monitoring Post-Fire Forest Recovery. *Drones* **2019**, 3, 6.

Li., C., Zhou, L., Xu, W., 2021. Estimating aboveground biomass using Sentinel-2 MSI data and ensemble algorithms for glassland in the Shengjin Lake wetland, China. *Remote Sens*, 13(8), 15951613.

Lorenzen, B. Jensen, A., 1988. Reflectance of blue, green, red and near infrared radiation from wetland vegetation used in a model discriminating live and dead above ground biomass. *New Phytol*, 108, 345–355.

Louppe, G., Wehenkel, L., Sutera, A., Geurt, P., 2013. Understanding variable importances in forests of randomized trees. *Adv Neural Inf Process Syst*, 431–439.

Mallik, A.U., Wein, R.W. 1986. Response of a *Typha* marsh community to draining, flooding, and seasonal burning. *Can. J Botany*, 64(9), 2136¬2143, doi:10.1139/b86-282.

Martin, F.M., Müllerová, J., Borgniet, L., Dommanget, F., Breton, V., Evette, A. 2018 Using single-and multi-date UAV and satellite imagery to accurately monitor invasive knotweed species. *Remote Sens*, 10, 1662; doi:10.3390/rs10101662.

Meng, X., Shang, N., Zhang, X., Li, C., Zhao, K., Qiu, X., and Weeks, E., 2018. Photogrammetric UAV mapping of terrain under dense coastal vegetation: an object-oriented classification ensemble algorithm for classification and terrain correction. *Remote Sens*, 9(11), 11871210

Mishra, V.N., Prasad, R., Rai, P.K., Vishwakarma, A.K., Arora, A., 2018. Performance evaluation of textural features in improving land use/land cover classification accuracy of heterogeneous landscape using multi-sensor remote sensing data. *Earth Sci Inform*, 12, 71–86.

Mury, A., Collin, A., Houet, T., Alvarez-Vanhard, E., James, D. 2020. Using multispectral drone imagery for spatially explicit modeling of wave attenuation through a salt marsh meadow. *Drones*, 4, 25, doi:10.3390/drones4020025.

Nardin, W., Taddia, Y., Quitadamo, M., Vona, I., Corbau, C., Franchi, G., Staver, L.W., Pellegrinelli, A., 2021. Seasonality and characterization mapping of restored tidal marsh by NDVI imageries coupling UAVs and multispectral camera. *Remote Sens*, 13, 42074226.

Norris, G.S., Meed, N.R., Barbeau, M.A., Ollerhead, J., McLellan, N.R., 2020. Restoration of salt marsh in a former freshwater impoundment in Musquash, NB: the first year after breaching the dike. Department of Biology, University of New Brunswick, Fredericton, NB. Report for Ducks Unlimited Canada for 2019, 48.

Ok, A.O., Akar, O., Gungor, O. 2012. Evaluation of random forest method for agricultural crop classification. *European Journal of Remote Sens*, 45(1), 421-432.

Pajares, H., 2015. Overview and current status of remote sensing applications based on unmanned aerial vehicles (UAVs). *Photogramm Eng Rem S*, 81(4), 281–329.

Peñuelas, J., Filella, I., 1998. Visible and near infrared reflectance techniques for diagnosing plant physiological status. *Trends Plant Sci*, 3, 151–156.

Richards, J.A., Jia, X. 1999. Remote sensing digital image analysis: an introduction. Springer. New York. ISBN 978-3-642-30062-2.

Ridge, J.T., Johnston, D.W., 2020. Unoccupied Aircraft Systems (UAS) for marine ecosystem restoration. *Front Mar Sci*, 7(438).

Roman, C.T., Burdick, D.M., 2012. Tidal Marsh Restoration: A Synthesis of Science and Management. Society of Ecological Restoration. Island Press, Washington.

Sarira, T.V., Clarke, K., Weinstein, P., Koh, L.P., Lewis, M. 2020. Rapid identification of shallow inundation for mosquito disease mitigation using drone-derived multispectral imagery. *Geospatial Health*, 15(1), doi:10.4081/gh.2020.851.

Strobl, C., Boulesteix, A.L., Kneib, T., Augustin, T., Zeileis, A., 2008. Conditional variable importance for Random Forests. BMC Bioinfor, 9, 307.

Thomas, M.L.H., 1983. Salt marsh systems. In: *Marine and Coastal Systems of the Quoddy Region, New Brunswick*. Department of Fisheries and Oceans, 64, 107–118.

Thompson, D.H., 2001. Settlements and Landscapes of the Musquash Estuary: Past and Present. Report prepared in support of Musquash Marine Protected Area Campaign. Conservation Council of New Brunswick, 18 pg.

van Beijma, S., Comber, A., Lamb, A., 2014. Random forest classification of salt marsh vegetation habitats using quad-polarimetric airborne SAR, elevation and optical RS data. *Remote Sens Env*, 149, 118129.

Villoslada, M., Bergamo, T.F., Ward, R.D., Burnside, N.G., Joyce, C.B., Bunce, R.G.H., Sepp, K., 2020. Fine scale plant community assessment in coastal meadows using UAV based multispectral data. *Ecol Indic*, 111, 105979–105992.

Virgin, S.D.S., Beck, A.D., Boone, L.K., Dykstra, A.K., Ollerhead, J., Barbeau, M.A., McLellan, N.R. 2020. A managed realignment in the upper Bay of Fundy: community dynamics during salt marsh restoration over 8 years in a megatidal ice-influenced environment. *Ecol Eng*, 149(105713).

Wan, H., Wang, Q., Jiang, D., Fu, J., Yang, Y., Liu, X. 2014. Monitoring the invasion of *Spartina alterniflora* using very high resolution unmanned aerial vehicle imagery in Beihai, Guangxi (China). *The Scientific World Journal*, 638296, doi:10.1155/2014/638296.

Waske, B., Braun, M., 2009. Classifier ensembles for land cover mapping using multitemporal SAR imagery. *ISPRS J Photogramm*, 64 (5), 450-457.

Xu, Z., Shen, X., Cao, L., Coops, N.C., Goodbody, T.R.H., Zhong, T., Zhao, W., Sun, Q., Ba, S., Zhang, Z., Wu, X., 2020. Tree species classification using UAS-based digital aerial photogrammetry point clouds and multispectral imageries in subtropical natural forests. *Int J Appl Earth Obs*, 92(102173), https://doi.org/10.1016/j.jag.2020.102173.